Electrochimica Acta 388 (2021) 138544

Contents lists available at ScienceDirect

Electrochimica Acta

journal homepage: www.elsevier.com/locate/electacta

Kinetics studies of thin film amorphous titanium niobium oxides for lithium ion battery anodes

Charles A. Hall[a,*], Yu Jiang[a], Patrick A. Burr[b], Shujuan Huang[a], Zhi Li Teh[a], Ivan Perez-Wurfl[a], Ning Song[a], Alison Lennon[a]

[a] *School of Photovoltaic and Renewable Energy Engineering, UNSW Sydney, NSW 2052, Australia*
[b] *School of Mechanical and Manufacturing Engineering, UNSW Sydney, NSW 2052, Australia*

ARTICLE INFO

Article history:
Received 15 October 2020
Revised 26 April 2021
Accepted 2 May 2021
Available online 15 May 2021

Keywords:
High-rate energy storage
Potentiostatic intermittent titration technique (PITT)
Amorphous titanium niobium oxide
Diffusion coefficient
Insertion reaction kinetics

ABSTRACT

Amorphous titanium niobium oxides (TNOs) with varying ratios of Ti and Nb ($Ti_4Nb_2O_{13}$, $Ti_2Nb_2O_9$ and $TiNb_2O_7$) are presented as promising anode materials for Li ion batteries. The capacity of the TNO materials is seen to be equivalent to, or larger than, that of the binary oxides, with average volumetric capacities over the first 10 cycles of 717, 1,039 and 925 mAh cm^{-3} for amorphous $Ti_4Nb_2O_{13}$, $Ti_2Nb_2O_9$ and $TiNb_2O_7$, respectively at a current density of 0.2 A cm^{-3}, compared to 720 mAh cm^{-3} and 425 mAh cm^{-3} for amorphous TiO_2 and Nb_2O_5. Using densities estimated with X-ray reflectometry, these are equivalent to gravimetric capacities of 231, 335, 319 mAh g^{-1} for amorphous $Ti_4Nb_2O_{13}$, $Ti_2Nb_2O_9$ and $TiNb_2O_7$, respectively at a current density of ~70 mA g^{-1}, compared to 257 mAh g^{-1} and 137 mAh g^{-1} for amorphous TiO_2 and Nb_2O_5 at a current density ~80 mA g^{-1} and ~50 mA g^{-1}, respectively. We discuss how rate capability varies with varying ratios of Ti and Nb and relate this to electrochemical parameters determined by the potentiostatic intermittent titration technique. Our findings reveal that the rate capability of the films is dominated by the diffusion resistance, R_D, a composite parameter linked to the insertion rate and diffusion coefficient of Li, leading to a conclusion that the rate retention of the thin films is dominated by the density of insertion sites and the insertion reaction more generally.

© 2021 Elsevier Ltd. All rights reserved.

1. . Introduction

Applications for electrochemical energy storage systems which can be rapidly charged and discharged are growing, particularly in the areas of electric vehicles and grid connected intermittent renewable energy [1,2]. High rate lithium ion batteries (LIBs) have the potential to fill this need due to the ability of the Li ions to intercalate or alloy rapidly in solid electrode materials [3,4]. However the commonly-used graphite anodes have a Li insertion potential that is close to that of the Li plating (reduction) potential and this presents the critical challenges of solid electrolyte interphase (SEI) growth and dendritic Li growth at fast rates of charging [5–7]. Promising alternatives to conventional graphite which have a higher lithiation potential and exhibit similar or greater capacity, but greatly improved rate capability, include spinel lithium titanate (LTO) [8], TiO_2 [9–11], titanium niobium oxide ($Ti_2Nb_{2x}O_{4+5x}$; TNO) [12,13], niobium tungsten oxide ($Nb_xW_yO_{2.5x+3y}$; NWO) [14] and Nb_2O_5 [15,16].

The TiO_2_Nb_2O_5 (TNO) system shows particular promise. This includes $TiNb_2O_7$, $Ti_2Nb_2O_9$, $Ti_2Nb_{10}O_{29}$ and $TiNb_{24}O_{62}$. The further phases of TiO_2•$3Nb_2O_5$ and TiO_2•$7Nb_2O_5$ may also be possible, however there exists some debate about whether these are stable phases, or mixtures of the aforementioned phases [17,18]. These TNO materials exhibit: (i) electroactivity in the operational potential window of 1–3 V vs Li^+/Li; (ii) fast Li diffusion, allowing them to operate at high lithiation and delithiation rates; and (iii) a capacity greater than LTO, and in some cases greater than graphite. The theoretical specific capacities, the rate capability (i.e., capacities at ~ 1 and ~ 20C) and the chemical diffusion coefficients of various TNO materials are shown in Table S1, with comparisons to better-known materials (e.g., graphite, LTO, TiO_2, NWO, Nb_2O_5). The TNO materials exhibit greater specific capacity ~ 1C than LTO and comparable specific capacities at rates ~ 20C. The theoretical capacity of the TNO materials ranges from 335.8 mAh g^{-1} (pure TiO_2) to 403.2 mAh g^{-1} (pure Nb_2O_5) assuming one Li is inserted per Ti and two Li are inserted per Nb [19,20]. These values are comparable to graphite, which has a theoretical specific capacity of 372 mAh g^{-1} (assuming 1 Li per C_6) [21]. The crystal phases of TNO materials allow comparable or greater Li chemical diffu-

---

[*] Corresponding author.
E-mail address: charles.hall@unsw.edu.au (C.A. Hall).

https://doi.org/10.1016/j.electacta.2021.138544
0013-4686/© 2021 Elsevier Ltd. All rights reserved.

sion coefficients, D_{Li}, than that of LTO, for which values range from 2.2×10^{-16} to 8.2×10^{-16} cm^2 s^{-1} [22], 10^{-12} to 10^{-10} cm^2 s^{-1} [23], 10^{-15} to 10^{-12} cm^2 s^{-1} (see Table S1) [24]. A range of D_{Li} values have also been reported for various TNO forms: these include 10^{-16} to 10^{-15} cm^2 s^{-1} for $TiNb_2O_7$ [25], 10^{-12} cm^2 s^{-1} for $Ti_2Nb_2O_9$ [26], 5×10^{-14} to 1.2×10^{-12} cm^2 s^{-1} for $Ti_2Nb_{10}O_{29}$ [27], and 10^{-14} to 10^{-10} cm^2 s^{-1} for $TiNb_{24}O_{62}$ [18].

However, the storage of Li in amorphous forms of TNO hasn't been investigated in detail. At one extreme, amorphous TiO_2 shows improved capacity at high rates of de/lithiation and faster Li diffusion, when compared to crystalline TiO_2 polymorph [28–30]. Whereas amorphous Nb_2O_5 exhibits lower capacity at high rates of de/lithiation and slower Li diffusion in comparison to crystalline Nb_2O_5 polymorphs [16]. Recently, Daramalla et al. [31] reported an amorphous $TiNb_2O_7$ film that showed improved capacity over the crystalline (monoclinic) $TiNb_2O_7$, however comparable rate capability and diffusion coefficients to the crystalline $TiNb_2O_7$. This suggests that benefits in either rate capability or capacity that may arise from amorphous films of this class of anode materials over their crystalline counterparts depend on the chemical composition, stoichiometry and thermodynamically stable material phases.

In this paper we investigate how varying ratios of Nb to Ti affect the kinetic properties of selected TNO amorphous thin films. Of particular interest were: (i) film capacity and rate capability; (ii) film interfacial reaction kinetics; and (iii) Li diffusion in the films. Amorphous thin films of $Ti_2Nb_{2x}O_{4+5x}$ were fabricated using sol-gel synthesis methods to result in a stoichiometry closely matching their precursor sols (i.e. TiO_2, $Ti_4Nb_2O_{13}$, $Ti_2Nb_2O_9$, $TiNb_2O_7$, and Nb_2O_5). In particular, we investigated how the ratio of Ti and Nb in amorphous TNO affects capacity, capacity retention at high rates of de/lithiation and electrochemical parameters associated with Faradaic and physical charge storage processes (i.e., the charge transfer and diffusion behaviour, and double layer storage, respectively). The findings of this study provide further support for the use of amorphous TNO materials in alternative Li ion battery anodes. The amorphous $Ti_2Nb_2O_9$, $TiNb_2O_7$ films show improved capacity over both of the amorphous end-members (TiO_2 and Nb_2O_5) at rates below 10C, however the chemical diffusion coefficient and capacity retention at high rates for all of the TNO films are reduced compared to amorphous TiO_2 or Nb_2O_5.

2. Experimental

2.1. Sol gel synthesis

Thin films of $Ti_2Nb_{2x}O_{4+5x}$, TiO_2, and Nb_2O_5 were fabricated via the sol gel method. The Ti and Nb sols were prepared based on synthesis described elsewhere [32–35] in an Ar filled glovebox. The Ti sol was prepared by mixing 6 drops HCl (RCI Labscan; 32%), 0.35 mL deionised (DI) water and 10 mL 1-butanol (Sigma Aldrich; Anhydrous 99.8%), and then adding 0.75 mL (0.325 M) of Ti ethoxide (Sigma Aldrich) dropwise while the solution was stirring, following by stirring for a further 24 h. The Nb sol was prepared by mixing 4.823 mL 1-butanol and 51.3 µL acetyl acetone (Sigma Aldrich; >=99%), and then adding 125.5 µL (0.1 M) Nb ethoxide (Sigma Aldrich; 99.95%) dropwise under constant stirring, followed by stirring for a further 2 h. Mixed Ti-Nb sols were prepared by mixing stoichiometric amounts of Ti and Nb sols (2:1, 1:1, and 1:2 molar ratios Ti:Nb) in an Ar filled glovebox for 1 h under constant stirring. The mixed sols became a light shade of yellow, in contrast to the Ti and Nb sols which were colourless, as the Ti ethoxide reacted with the acetyl acetone [36]. After synthesis, all sols were kept in a refrigerator at 4 °C.

2.2. Metal oxide thin film deposition

Thin films were formed on 30 × 30 × 0.015 mm Al foils (MTI) by spin coating the sols at 3000 rpm for 60 s in air. Prior to spin coating, the Al films were cleaned ultrasonically for 10 min each in acetone (Ajax-Finchem), IPA (Ajax-Finechem) and then DI water. The native Al oxide was then removed by an acid etch, modified from a method described by Von Heimendahl [37] as described by Walker and Tarn [38], containing 35:10:3 H_3PO_4:HNO_3:DI water for 30 s. The H_3PO_4 was sourced from BASF (85%) and the HNO_3 was sourced from RCI Labscan (70%). The cleaned Al foil was taped to polished Si wafers, to ensure the surface was as flat as possible whilst spin coating. All films were prepared with only one spin coating, to ensure that films were as thin as possible. The films were dried at 115 °C for 20 min on a hotplate, followed by annealing in air. For amorphous TNO films, annealing was performed at 250 °C for 2 h. For comparison, some TiO_2 films were annealed to form anatase TiO_2. These films were annealed at 500 °C for 2 h. Six types of thin film were prepared: amorphous and crystalline TiO_2 (designated a-TiO_2 and c-TiO_2, respectively), amorphous TNO films with Ti:Nb ratios of 2:1, 1:1 and 1:2 (designated a-$Ti_4Nb_2O_{13}$, a-$Ti_2Nb_2O_9$, and a-$TiNb_2O_7$) and amorphous Nb_2O_5 (designated a-Nb_2O_5).

2.3. Material characterisation

The thin film morphology and thickness was characterized with field emission scanning electron microscopy (FE-SEM) (FEI Nova NanoSEM) operating with a source emission at 5 kV. It was not possible to measure the mass of the films accurately, as the film mass was within the standard deviation of the mass of the foil current collectors. Consequently, the thicknesses of the films were measured with SEM, by bending the underlying Al foil, which resulted in the film cracking and peeling from the foil. Thicknesses were measured from multiple films and in multiple locations on the foil.

Film homogeneity and crystallinity was characterized with transmission electron microscopy (TEM) (Phillips CM200; operating at 200 kV) of lamellas made with a Ga source dual-beam focused ion beam (FIB) (FEI xT Nova Nanolab). Prior to making any lamella sections with FIB, the surface was coated with Pt. The Pt coating was performed in two steps to avoid beam damage: firstly, before the ion beam was used, a ~20 nm Pt coating was applied with the electron beam, and secondly a several micron thick Pt layer was applied using the ion beam. The chemical composition of the films was characterized using X-ray photoelectron spectroscopy (XPS) (Thermo Scientific ESCALAB250Xi) with a mono-chromated Al Kα source (1486.68 eV) and spot size of 500 µm. The presence of crystal structure was characterized with X-ray diffraction (XRD) (PANalytical Empyrean 1). The density of the films was determined via X-ray reflectometry (XRR) (PANalytical MRD diffractometer; 1/8 inch divergence slit, 1.2 mm mask). All density measurements were made with films spin coated onto polished Si wafers (20 mm × 20 mm × 500 µm). Prior to spin coating, wafers were cleaned for 10 min in acetone and IPA, and then the native oxide was removed by a 30 s immersion in HF. Drying and annealing was conducted as it was for Al substrates.

2.4. Electrochemical methods

Electrochemical characterization of the thin films was performed using Li half cells assembled in a CR2032 coin cell case (MTI), comprising a Li counter electrode (Xiamen TMAX Li; 16 mm diameter × 450 μm) and the thin films on Al foil as a working electrode (15 mm diameter). The electrolyte comprised of 1 M $LiPF_6$ in ethylene carbonate and ethyl methyl carbonate

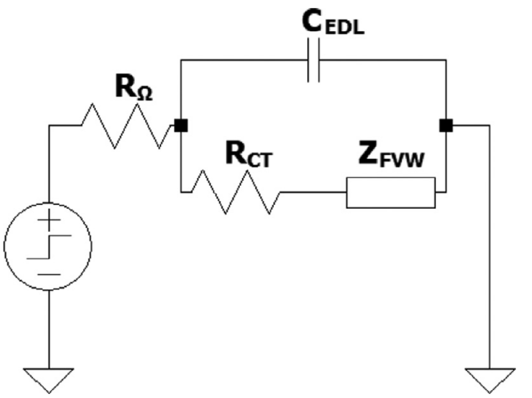

Fig. 1. Equivalent circuit used for fitting PITT experimental data. A modified version of this equivalent circuit used for fitting EIS experimental data is shown in Fig. S16.

(1:1) sourced from Sigma Aldrich. The separator (Celgard, 25 μm polypropylene) was made slightly larger than the Li disk or working electrode. All cells were assembled in an Ar filled glovebox (O_2 and H_2O $<$ 0.5 ppm) using 80 μL of electrolyte, with half of the electrolyte placed on either side of the separator.

All electrochemical measurements were performed using an Ivium potentiostat (either IviumStat or Ivium-n-Stat). Prior to measurement, all cells were prelithated for two lithiation and delithiation cycles at a constant current of 1 μA across the potential range 3.0 to 1.0 V vs Li^+/Li (~ 1 dis/charge per 10 h). The cells were cycled at a constant current from 1.0 to 3.0 V vs Li^+/Li at current densities from ~200 mA cm^{-3} to ~200 A cm^{-3}, followed by cyclic voltammetry from 1.0 to 3.0 V vs Li^+/Li at voltage scan rates ranging from 1 mV s^{-1} to 150 mV s^{-1}.

Electrochemical parameters were determined using the potentiostatic intermittent titration technique (PITT) [39,40] and electrochemical impedance spectroscopy (EIS). The PITT protocol involved 100 mV steps from 3.0 to 1.0 V vs Li^+/Li and then back to 3.0 V. To collect very short time scale data, two sets of measurements were made. The first step recorded the current transient of the 100 mV step at a 10 μs frequency over 5 ms. The electrode was then stepped back to the previous potential and held for 10 s, followed by a repetition of the potential step with a measurement frequency of 1 ms, over a period of 100 s.

2.5. Electroanalytical models for PITT and EIS

The Li ion insertion properties of the films were analysed using the PITT and EIS data. Previously derived models were used for concurrent double layer storage and insertion of a species into a thin film (viz. finite length bounded diffusion) [41]. The equivalent circuit used for fitting PITT experimental data is shown in Fig. 1; a slightly modified equivalent circuit used for fitting EIS experimental data is shown in Fig. S16. Both of these models allow, through fitting of experimental data, the determination of: (i) the double layer capacitance C_{EDL}; (ii) the lumped ohmic resistance R_Ω; (iii) the charge transfer resistance R_{ct}; (iv) the diffusion resistance R_D; and (v) the chemical diffusion coefficient D_{chem}. Throughout this paper we use the term electrochemical parameters to refer to these estimated parameters collectively.

Of these, the values of R_{ct} and R_D are regularly reported as kinetic parameters, but R_D is rarely attributed to physical processes. Here, to model the insertion of Li into a thin film, we use the interpretation presented by Montella [42] which assumes the insertion reaction occurs as $Li^+ + e^- \leftrightarrow Li_{ins}$ and not via an adsorbed intermediate. This interpretation also assumes that the concentration of Li^+ in the electrolyte is constant in the region of the film, and that the insertion rate follows that of the Langmuir intercalation isotherm; that is, the insertion rate depends on the concentration of free sites and the electrode potential, E. The value of R_{ct} is then given by:

$$R_{ct} = -\frac{1}{F\ A\frac{\partial v}{\partial E}} \tag{1}$$

where F is Faraday's constant, A is surface are of the film and $\frac{\partial v}{\partial E}$ is the partial derivative of reaction rate, v, with respect to E [42,43]. Here, we interpret R_{ct} as a kinetic parameter relating to the value of E required to insert or extract Li in the reaction $Li^+ + e^- \leftrightarrow Li_{ins}$. The value of R_D is given by:

$$R_D = \frac{L\ \frac{\partial v}{\partial c}}{FD_{chem}\ A\frac{\partial v}{\partial E}} \tag{2}$$

where L is the thickness of the film, and $\frac{\partial v}{\partial c}$ is the partial derivate of reaction rate, v, with respect to the concentration, c, of inserted Li at the surface of the film [42,43]. We interpret R_D as a mixed parameter, relating to both the diffusion of Li and the kinetics of the insertion of Li, which is in part governed by both E and the concentration of occupied surface sites, as well as the diffusivity.

The impedance for the equivalent circuit shown in Fig. 1 is:

$$Z(j\omega) = R_\Omega + \frac{1}{j\omega\ C_{EDL} + \frac{1}{R_{ct} + \frac{R_d\ \coth\sqrt{\tau\ j\omega}}{\sqrt{\tau\ j\omega}}}} \tag{3}$$

and the corresponding time domain equation for the current transient where this equivalent circuit undergoes a potential step [41] is:

$$I(t) = \sum_{n=1}^{\infty} \frac{2\ R_d \Delta E}{\begin{pmatrix} f(x_n)^2\ R_d\ (R_{ct} + R_d) \\ + \\ (2 - f(x_n))\ R_d R_\Omega \\ + \\ (f(x_n)\ R_{ct} + R_\Omega)^2 {x_n}^2 \end{pmatrix}} e^{\frac{-t\ {x_n}^2}{\tau}} \tag{4}$$

where:

$$f(x) = \left(1 - \frac{C_{EDL}\ R_\Omega\ x^2}{\tau}\right) \tag{5}$$

and the values of x_n for $n = 1,\ 2,\ 3,\ \ldots\infty$ are found by solving the transcendental roots of:

$$x \tan x = \frac{R_d\ f(x)}{R_\Omega +\ R_{ct}\ f(x)} \tag{6}$$

2.6. Normalisation of rate retention data

The analysis of rate performance data presented by Tian et al. [44] was used to provide an estimate for the maximum attainable capacity when cycled at a low rate, $Q_{low\ rate}$, for each cell. This approach involves fitting the equation to the galvanostatic charge-discharge experimental data for each TNO film:

$$Q_{measured}\ =\ Q_{low\ rate}\left(1 - \left(\bar{R}\bar{\tau}\right)^n\left(1 -\ e^{-\left(\bar{R}\bar{\tau}\right)^{-n}}\right)\right) \tag{7}$$

where $Q_{measured}$ is the measured gravimetric capacity at a given rate of discharge $\bar{R}$ (i.e. $\bar{R} =\ I/Q_{measured}$), $\bar{\tau}$ is the characteristic time and n is a parameter related to the rate limiting behaviour. The fitting was performed using Matlab's nonlinear least squares fitting. As the aim of this fitting was to produce an estimate of $Q_{low\ rate}$, the target function of the least squares fitting contained the absolute error of the capacity at a given rate, rather than the relative errors. As a result, the fitting is seen to be poor in the high rate, low capacity regime. While it was possible to improve the fitting in the high rate regime by using the relative errors of the capacities instead of the absolute errors, the low rate regime was more accurately modelled so as to produce a more accurate estimate of $Q_{low\ rate}$.

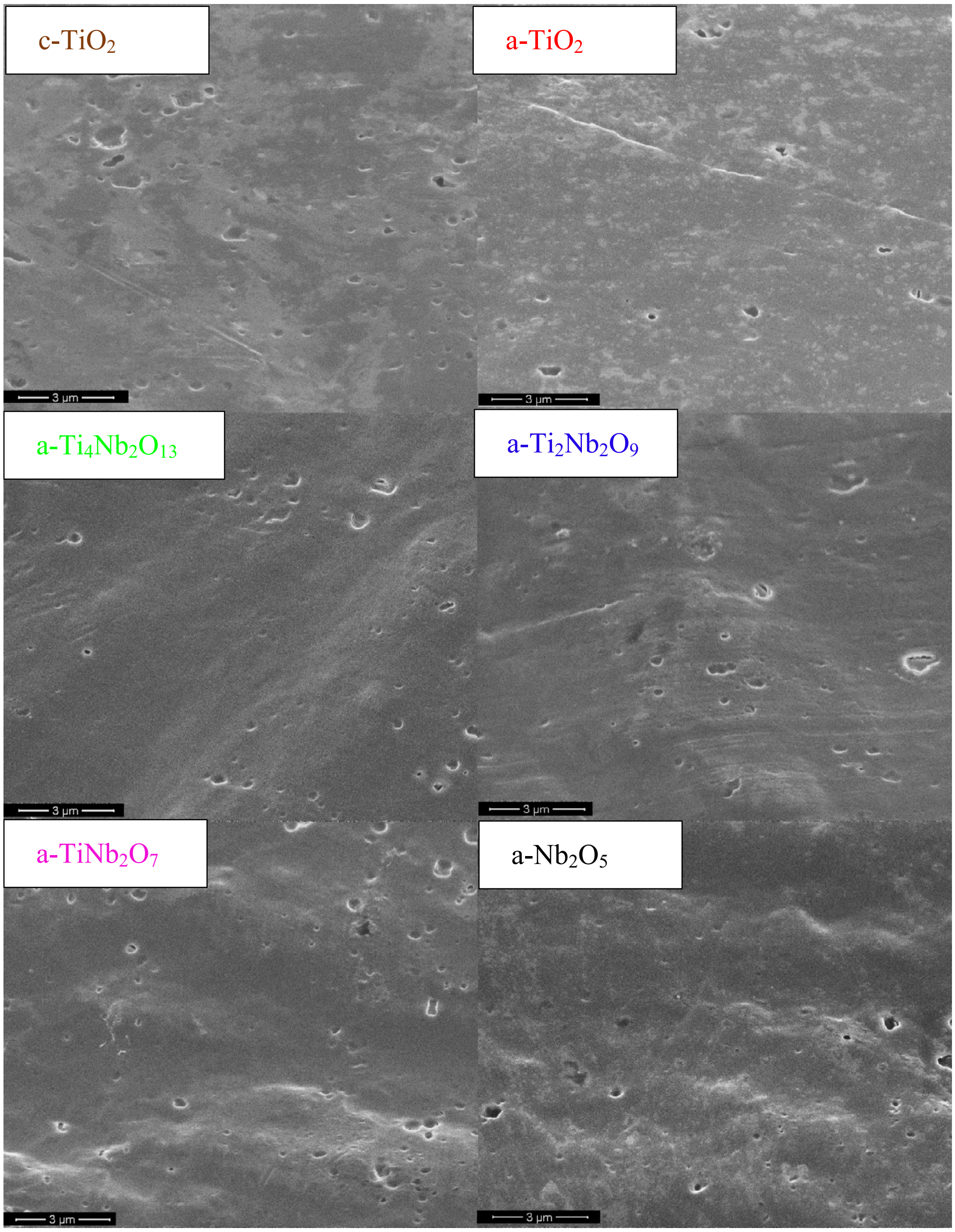

Fig. 2. Scanning electron microscope images of anatase and amorphous TiO_2, TNO films, and Nb_2O_5 deposited in Al foil current collectors, recorded at an angle of 45° to the surface.

2.7. Correlation of rate retention and electrochemical parameters

To identify which electrochemical parameters played a significant role in influencing the capacity retention at high rates of de/lithiation, Pearson correlation coefficients were calculated between the capacity retention (as a percentage of $Q_{\text{low rate}}$) of the films at various $\bar{R}$ and the electrochemical parameters C_{EDL}, R_{Ω}, R_{ct}, R_{D} and D_{chem}. These correlation coefficients, and the associated p-values were produced using Matlab's corrcoef function.

3. Results and discussion

3.1. Material characterisation of thin film metal oxides

The surface morphology of the TNO thin films deposited on the Al foil current collectors is shown in Fig. 2. The SEM images were recorded at an angle of 45° to accentuate the features of the film morphology. All the TNO films have a smooth surface and very little particle formation, with the exception of the a-Nb_2O_5 where discrete aggregated particles were evident on the surface (Fig. S1). Film thicknesses ranged between 33 and 64 nm (see Table 1). As the aim of this paper was to study the diffu-

Table 1
Thicknesses of spin-coated and dried TNO films, as estimated using SEM. The standard deviation was calculated from 6 independent measurements.

	Thickness (nm) ± STD
TiO_2	64 ± 30
$Ti_4Nb_2O_{13}$	52 ± 8
$Ti_2Nb_2O_9$	33 ± 5
$TiNb_2O_7$	36 ± 7
Nb_2O_5	59 ± 11

sion behaviour in thin films using electroanalytical models for restricted diffusion, the films had to be sufficiently thin so as to observe restricted diffusion in PITT and EIS experiments. For restricted diffusion behaviour to be apparent in PITT experiments on a timescale of < 100 s (where the charge transfer occurs fast enough that the behaviour doesn't deviate from semi-infinite diffusion), a thickness of ~ 30 nm requires that the diffusion coefficient is $> 2 \times 10^{-14}$ cm s^{-1} (or $> 8 \times 10^{-14}$ cm s^{-1} for a thickness of ~ 60 nm) [42]. Similarly, for characteristic low frequency behaviour of restricted diffusion to be evident in EIS experiments at frequencies $\langle$ 1 mHz, the diffusion coefficient must be $\rangle$ 1.8×10^{-14} cm s^{-1} for a film thickness of ~ 30 nm (or $> 6.6 \times 10^{-14}$ cm s^{-1} for a thickness of ~ 60 nm) [43].

Fig. 3 shows TEM high-angle annular dark field (HAADF) images for a-$Ti_4Nb_2O_{13}$, a-$Ti_2Nb_2O_9$, and a-$TiNb_2O_7$ films. All film cross sections were prepared using FIB. No obvious phase segregation can be seen in the a-$Ti_4Nb_2O_{13}$, a-$Ti_2Nb_2O_9$ and a-$Ti_2Nb_2O_9$ films, suggesting that the spin-coated films remained homogenous in the nanometre scale rather than comprising stoichiometric fractions of TiO_2 and Nb_2O_5. The faint bright regions visible in the a-$TiNb_2O_7$ film could be due to FIB damage or porosity, but it is confirmed by EDX in Fig. 4 that there is an even distribution of Ti and Nb and so these regions are not due to phase separation.

The films annealed at 250 °C remained amorphous as shown in the XRD spectra shown in Fig. 5. The only visible XRD peaks are attributed to the Al substrate, which are common to all samples. The c-TiO_2 film, which was fabricated by annealing an a-TiO_2 film at 500 °C, showed a very minor peak shown corresponding to the (101) crystal plane of anatase [45], but remained largely amorphous (see Fig. S2). A TEM cross-section of the c-TiO_2 film is shown in Fig. S3. Unlike the amorphous films, subdomains of crystallinity are evident, however the crystallites appear to be <10 nm in size. This is consistent with previous reports which show that the speed of crystallisation of TiO_2 from an amorphous state is reduced with thinner films [46,47]. Additionally, it has been shown that sol gel derived TiO_2 thin films show increased crystallisation onset temperatures, over other synthesis methods [48].

The stoichiometries of the thin films were determined using XPS (see Figs. S4–S8). Binding energies were referenced to the C 1 s peak of adventitious hydrocarbon, which was assigned a binding energy of 284.8 eV. Two other major peaks were observed for the C 1 s orbital, at 286.4 and 289 eV. These were attributed to hydroxyl and carboxyl bonds, respectively, and thought to be products of the organic reactants of the sol gel synthesis [32]. Titanium atomic% was calculated based on the binding energy of the $2p_{3/2}$ orbital, which had a binding energy of 459.4 eV for the TiO_2 film and shifted to 459.0 in the TNO films. This is consistent with a Ti^{4+} valence state [49] which is consistent with other reports [32,33,35]. The Nb atomic% was attributed based on the $3d_{5/2}$ orbital, which was consistently between 207.0 and 207.8 eV across the samples. The valence state of the Nb was determined as previously reported [50] using the difference between the O 1 s and Nb $3d_{5/2}$ orbitals. Across all Nb-containing thin films, the energy difference between the O 1 s and Nb $3d_{5/2}$ was seen to be between 322.7 and 323.1 eV, which is consistent with a Nb^{5+} valence state [50]. The atomic% of O bonded to Ti and/or Nb was determined with the O 1 s orbital. Two O 1 s binding energies were observed across all samples; the first, dominant peak between 530.2 and 530.7 eV was attributed to binding between O and Ti or Nb [32], and the second between 532.0 and 532.3 eV was thought to be from hydrocarbons as part of the sol gel process [32].

Table 2
Stoichiometry of TNO films as determined from XPS, and density as determined from XRR.

Sol Stoichiometry	**Thin Film Stoichiometry**	**ρ (g cm^{-3})**
TiO_2	$TiO_{2.0}$	2.8 ± 0.1
$4TiO_2{\cdot}Nb_2O_5$	$Ti_4Nb_{2.2}O_{13.4}$	3.1 ± 0.1
$2TiO_2{\cdot}Nb_2O_5$	$Ti_2Nb_{2.4}O_{10.1}$	3.1 ± 0.1
$TiO_2{\cdot}Nb_2O_5$	$TiNb_{2.3}O_{8.0}$	2.9 ± 0.1
Nb_2O_5	$Nb_2O_{5.7}$	3.1 ± 0.1*

* Density estimated from $TiNb_{2.9}O_{8.9}$. Whilst the structure of $TiNb_{2.9}O_{8.9}$ is likely to be substantially different from Nb_2O_5, films with a higher Nb content showed local domains which rendered density estimates with XRR impossible (see comment in Supporting Information).

The stoichiometries, shown in Table 2, match closely with the stoichiometry of the sols used to fabricate the films. The pure Nb_2O_5 sample is seen to be hyper-stoichiometric. Various film stoichiometries fabricated from Nb_2O_5 sol gels have been reported, from hypo-stoichiometric [51], to stoichiometric [52,53], to hyper-stoichiometric (although this case was synthesised via spray pyrolysis, it involved the same solution chemistry) [54]. Table 2 also shows the density for the amorphous films, which was determined by fitting of XRR data. The density for Nb_2O_5 provided in Table 2 was estimated using density data for $TiNb_{2.9}O_{8.9}$, which was the most Nb rich TNO film that could be synthesised before the presence of local domains increased sufficiently that density estimates from XRR data were not possible (see comment in Supporting Information).

3.2. Electrochemical performance

Fig. 6 shows the CV curves recorded for the films at a scan rate of 1 mV s^{-1}. For consistency throughout this work, we have used volumetric current densities and capacities because, for some film stoichiometries (e.g., Nb_2O_5), accurate measurements of film density were difficult to obtain from the XRR analysis due to the presence of localised domains. Corresponding gravimetric CV data (computed using the estimated film densities) is shown at scan rates of 1, 10, 50, 100 and 150 mV s^{-1} in Figs. S9–S11 in the Supporting Information, along with volumetric CV data at a scan rate of 150 mV s^{-1}.

The c-TiO_2 shows a small set of cathodic and anodic peaks in the slow scan at 1.6 and 2.2 V vs Li^+/Li, respectively. These are attributed to a Ti^{4+} to Ti^{3+} transition and the reverse Ti^{3+} to Ti^{4+} transition (for the cathodic and anodic reaction, respectively) in the anatase domains and are consistent with previous reports [55–57]. The peaks however aren't sharp, and the shape resembles more closely that of a-TiO_2, which is consistent with the c-TiO_2 being only partly crystallised (see Figs. S2 and S3) [30]. The CV curve obtained for the a-TiO_2 film shows very broad peaks which indicate Li ion insertion over a wide range of potentials, as previously reported [28,30,58,59]. Broad peaks are also evident for the a-Nb_2O_5 and the TNO films. Similar broad peaks have also been reported by Ouendi et al. for a-Nb_2O_5 films [15]. The shape of the a-$TiNb_2O_7$ films matches that of the film reported by Daramalla et al. [31], with an increasing current towards 1 V vs Li^+/Li in the cathodic scan and a small peak at ~ 1.3 V vs Li^+/Li, and a very broad anodic peak at ~1.9 V vs Li^+/Li.

Fig. 7 graphs the volumetric capacities of the TNO films when cycled galvanostatically at current densities ranging from 0.2 to 2.1 A cm^{-3}. An explanation of why these current densities were used can be found in the Supporting Information. Galvanostatic charge discharge data for much higher current densities are also shown in the Supporting Information (see Fig. S12). Fig. S13 shows the gravimetric current densities computed using the film densities estimated by the XRR analysis and Table S2 lists the volumetric current densities for each material and their corresponding gravimetric current densities.

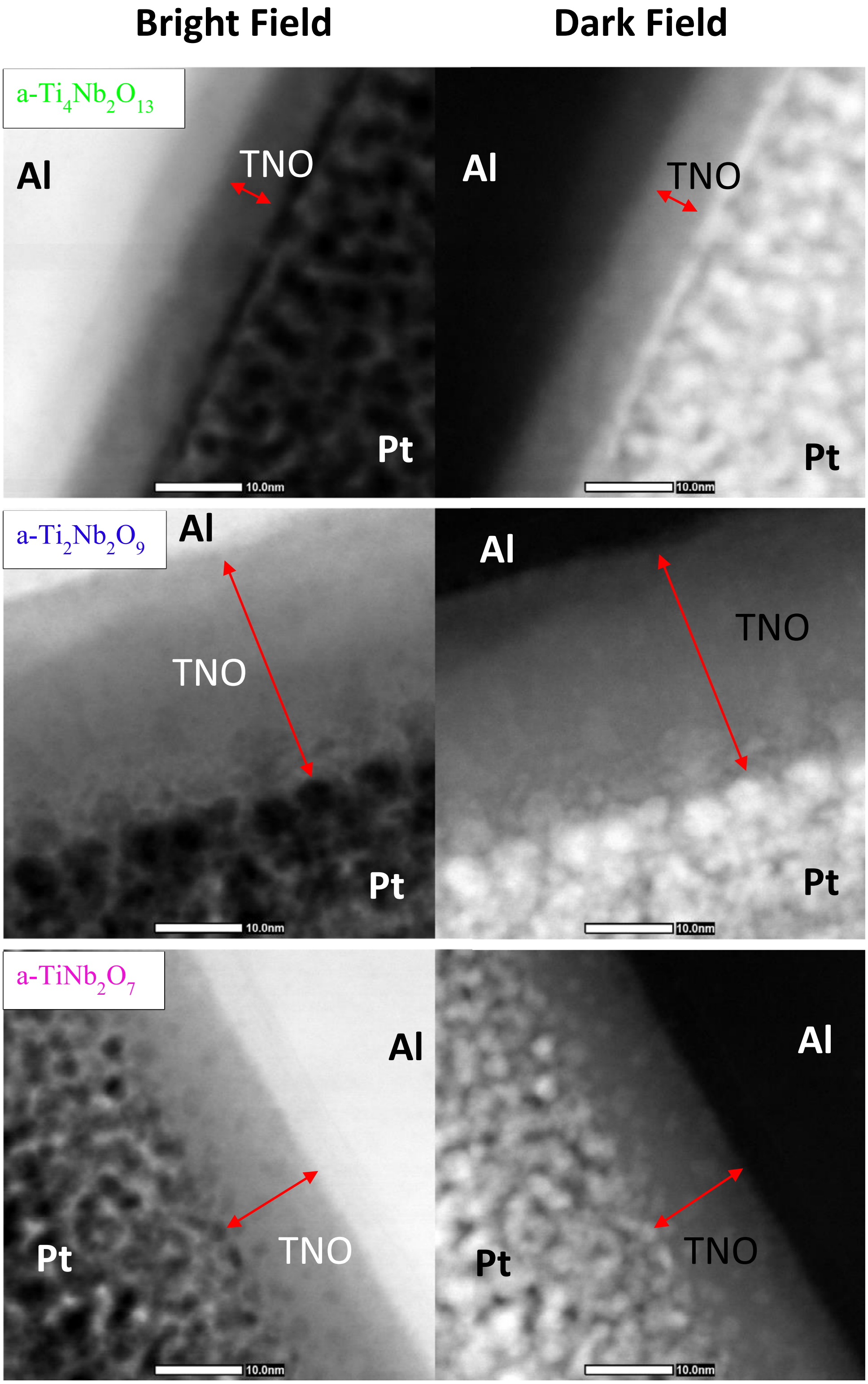

Fig. 3. High-angle annular dark field TEM images of the a-$Ti_4Nb_2O_{13}$ (top), a-$Ti_2Nb_2O_9$ (middle) and a-$TiNb_2O_7$ (bottom) spin coated thin films after annealing at 250 °C. Bright field images are displayed on the left for each of the TNO films, and dark field images are displayed on the right.

As can be seen in Figs. 7a and S12, the a-$Ti_2Nb_2O_9$, and a-$TiNb_2O_7$ films achieve higher volumetric capacities than the a-TiO_2 films for current densities $<$ 20 A cm^{-3}, however this advantage is reduced with increased current density. The a-$Ti_2Nb_2O_9$, and a-$TiNb_2O_7$ films show a mean capacity of 1039 mAh cm^{-3} and 925 mAh cm^{-3}, respectively over ten cycles at the lowest current density of 0.2 A cm^{-3} (equivalent to 335 mAh g^{-1} and 319 mAh g^{-1}, respectively at ~70 mA g^{-1}) compared to 720 mAh cm^{-3} and 425 mAh cm^{-3} at 0.2 A cm^{-3} for a-TiO_2 and a-Nb_2O_5, respectively (257 mAh g^{-1} at ~80 mA g^{-1} and 137 mAh g^{-1} at ~50 mA g^{-1}, re-

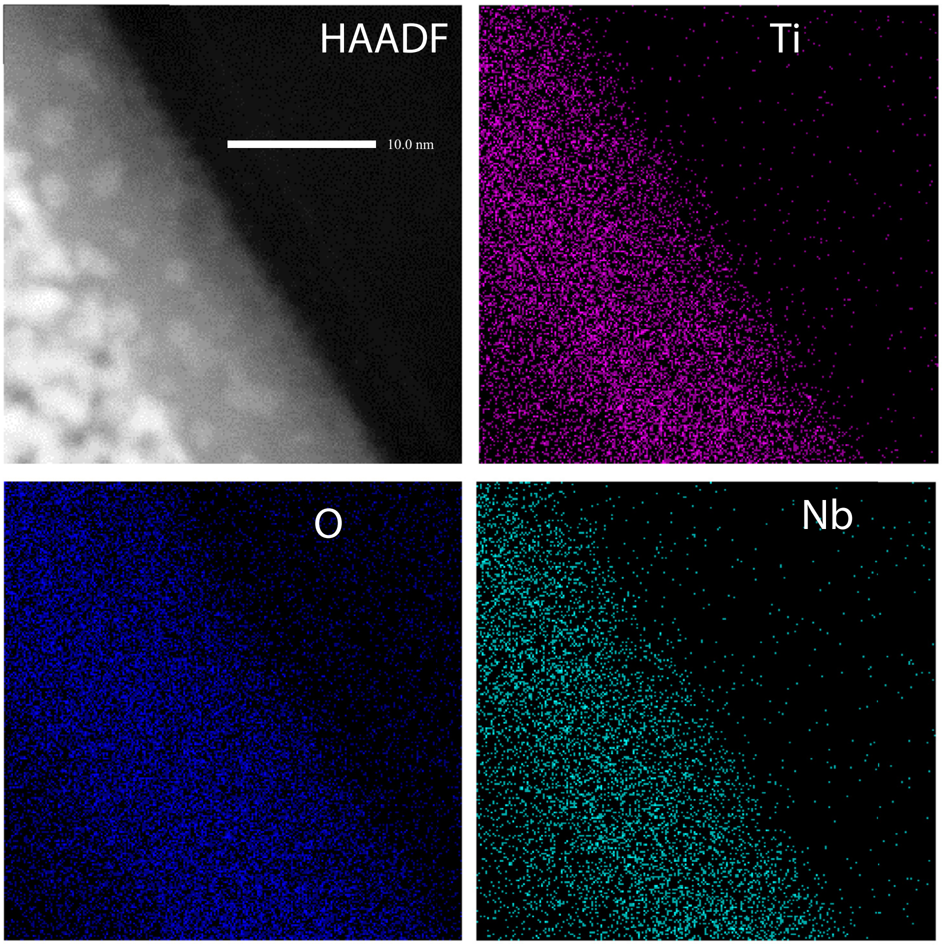

Fig. 4. Energy dispersive X-ray spectroscopy of a-$TiNb_2O_7$ after annealing at 250 °C, showing the element mapping for elements Ti, Nb and O. The Nb mapping was attributed using the Lα peak position, while Ti and O were attributed using the respective Kα peak positions.

spectively). That is to say, all of the amorphous ternary oxide films show comparable or greater volumetric capacity than the binary a-TiO_2 and a-Nb_2O_5.

The capacity-voltage curves of the amorphous films, shown in Fig. 7b, are featureless, further emphasising that Li ion insertion occurs over a range of potentials in these amorphous films. As in the CV data, the c-TiO_2 has a mixture of signature anatase insertion (with a lithiation and delithiation plateau ~ 1.7 and ~ 1.9 V vs Li^+/Li consistent with previous reports [57]) and broad, plateau-less behaviour typical of a-TiO_2. Despite two cycles of prelithiation at a low rate, the coulombic efficiency (CE) of the first 10 cycles was $<$ 95% for a number of the films (e.g. a-$Ti_2Nb_2O_9$ and a-$Ti_4Nb_2O_{13}$; see Fig. 7c). This was attributed to Li irreversibly intercalating into the film in early cycles. Beyond these first 10 cycles, the mean CE of all of the films was $>$ 97.5%, indicating that the films could be repeatably cycled for up to 100 cycles.

Whilst the broad peaks seen in CV data and near linear Q-V curves in galvanostatic charge discharge are frequently analysed using a b-value analysis to identify diffusive and capacitive contributions, we have elected not to use such terminology in large part due to concerns raised around its validity to systems such as ours [60]. Instead, the charge storage mechanisms (namely double layer storage and ion insertion storage) are analysed in greater detail in section 3.4.

Fig. 8a graphs the discharge capacity of the final cycle at each current density against the C rate (assuming a theoretical capacity based on 1 Li per Ti and 2 Li per Nb). Fig. 8b shows, for comparison, the capacities graphed as a function of gravimetric current density. At rates $<$ 10C, the a-$Ti_2Nb_2O_9$ shows the greatest capacity across all rates, retaining ~ 28% of the capacity of the slowest rate (~ C/5) at a rate of ~ 18C. However it is difficult to discern from Fig. 8 how the varying stoichiometry of the a-TNO films affects rate performance, and so instead we present a normalised rate performance in the next section.

3.3. Normalised rate retention

In order to determine rate retention at a given current density or C rate, a reference (e.g., capacity at 1C, C/10 etc.) must be selected. Since volumetric current densities were used for the constant current charge-discharge experiments, the lowest C rate varied between samples, making it difficult to quantitatively normalise the capacity retention data. Consequently, we estimated the maximum attainable capacity using the analysis of rate performance presented by Tian et al. [44] and then used this capacity to normalise rate retention in the films. This approach involves fitting Eq. (7) to the galvanostatic charge-discharge experimental data (details presented in Fig. S14). As with the data in Fig. 8, the last cycle of each current density was used for the analysis.

The thus-obtained estimates for $Q_{\text{low rate}}$ were then used to calculate the capacity retention from the maximum achievable capacity as a function of $\bar{R}$ (see Fig. 9). This normalisation shows that the a-TiO_2 film retains a larger fraction of its initial capacity than all of the other thin TNO films. Two distinct regimes can be seen

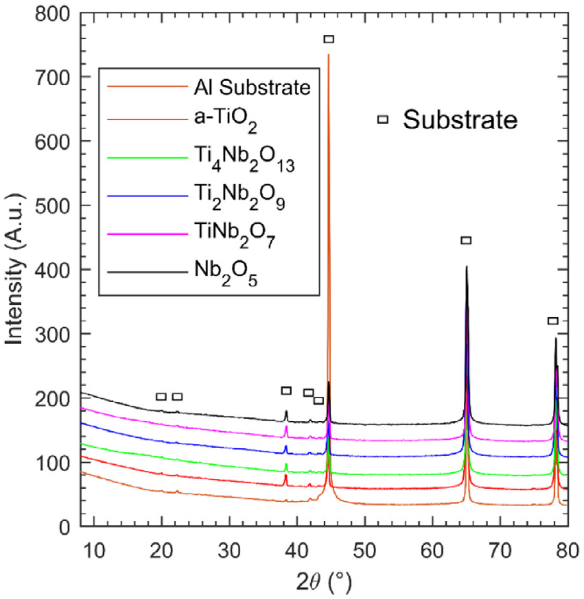

Fig. 5. X-ray diffraction spectra recorded for thin films of a-TiO_2 (64 nm), a-$Ti_4Nb_2O_{13}$ (52 nm), a-$Ti_2Nb_2O_9$ (33 nm), a-$TiNb_2O_7$ (59 nm), and a-Nb_2O_5 (59 nm) on Al foil after annealing at 250 °C, as well as a reference Al foil, which had also been annealed at 250 °C. The spectra show only the peaks of the background, indicating that the films are amorphous. The c-TiO_2 film is omitted here as it almost indistinguishable from a-TiO_2, and the differences between these samples are instead shown in Fig. S2.

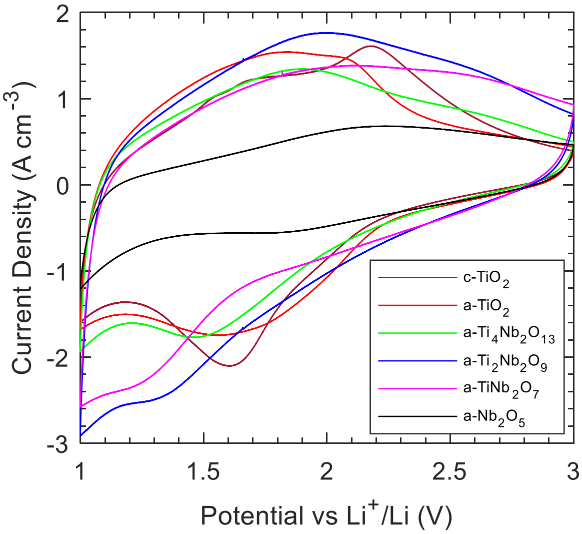

Fig. 6. Cyclic voltammetry curves measured for the TNO thin films at 1 mV s^{-1}.

across various rate scales. Firstly, at low to high rates ranging from $< 1\ h^{-1}$ to ~ 100–1000 h^{-1}, the order of capacity retention follows the film composition, with a-TiO_2 and c-TiO_2 retaining the most at a rate of 10 h^{-1} (52% and 50%, respectively), followed by a-$Ti_4Nb_2O_{13}$ (49%), a-$Ti_2Nb_2O_9$ (46%), a-$TiNb_2O_7$ (37%) and finally a-Nb_2O_5 (34%). This can be seen in Fig. 9b & c, which shows the rate retention at 1 and 10 h^{-1}. Secondly, at very high rates $> 1000\ h^{-1}$, the order of rate retention changes and whilst a-TiO_2 continues to

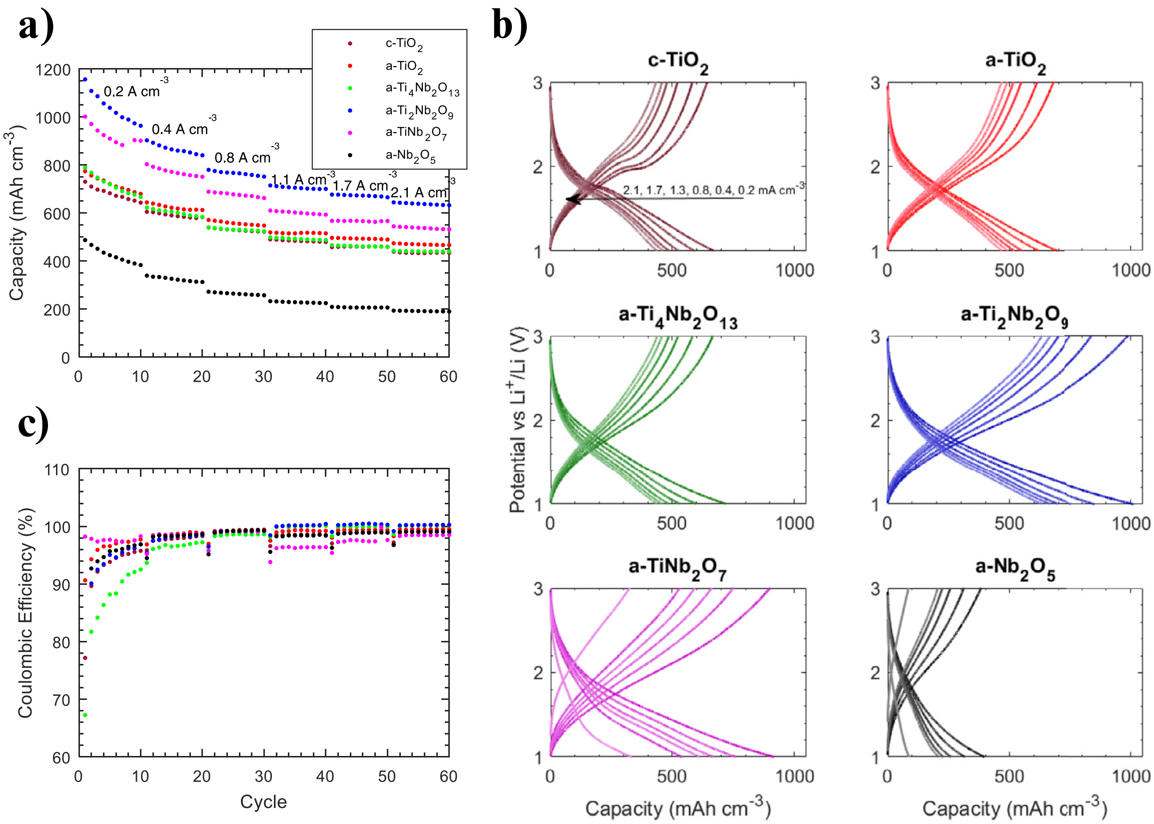

Fig. 7. Constant current charge discharge data at rates of 0.2, 0.4, 0.8, 1.3, 1.7 and 2.1 A cm^{-3} with (a) volumetric capacity as a function of current density; (b) representative charge-discharge curves, from the tenth cycle at each current density; and (c) the CE for the coin cells corresponding to the data in (a). Higher rate constant current charge discharge data are shown in Fig. S12.

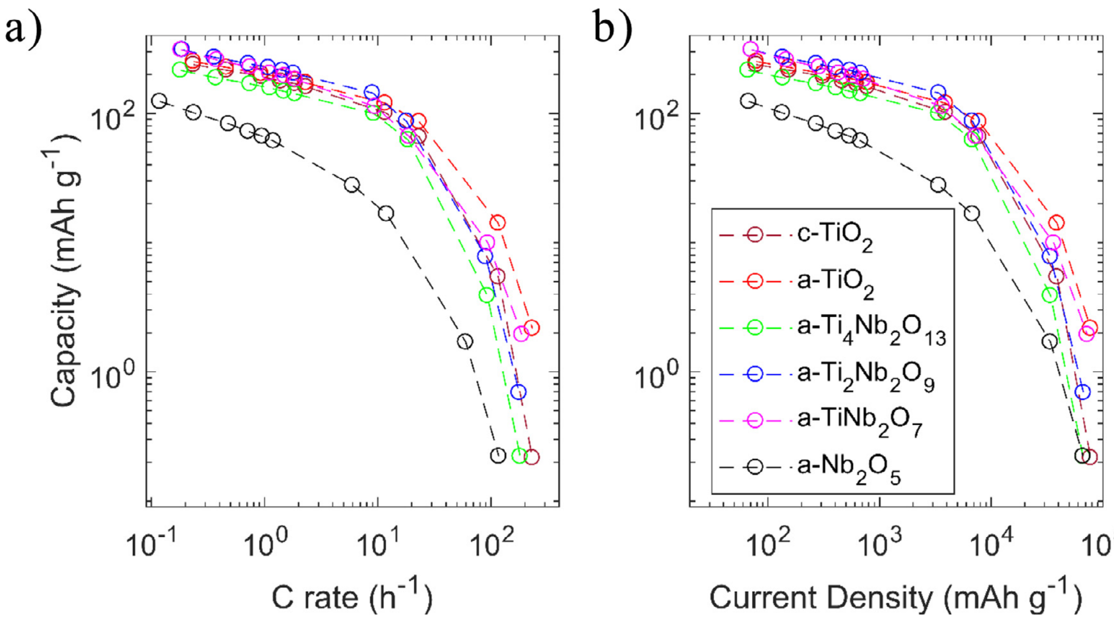

Fig. 8. Gravimetric capacity of TNO films as a function of C rate (a) and gravimetric current density (b). All C rates were calculated assuming a theoretical capacity based on 1 Li per Ti and 2 Li per Nb.

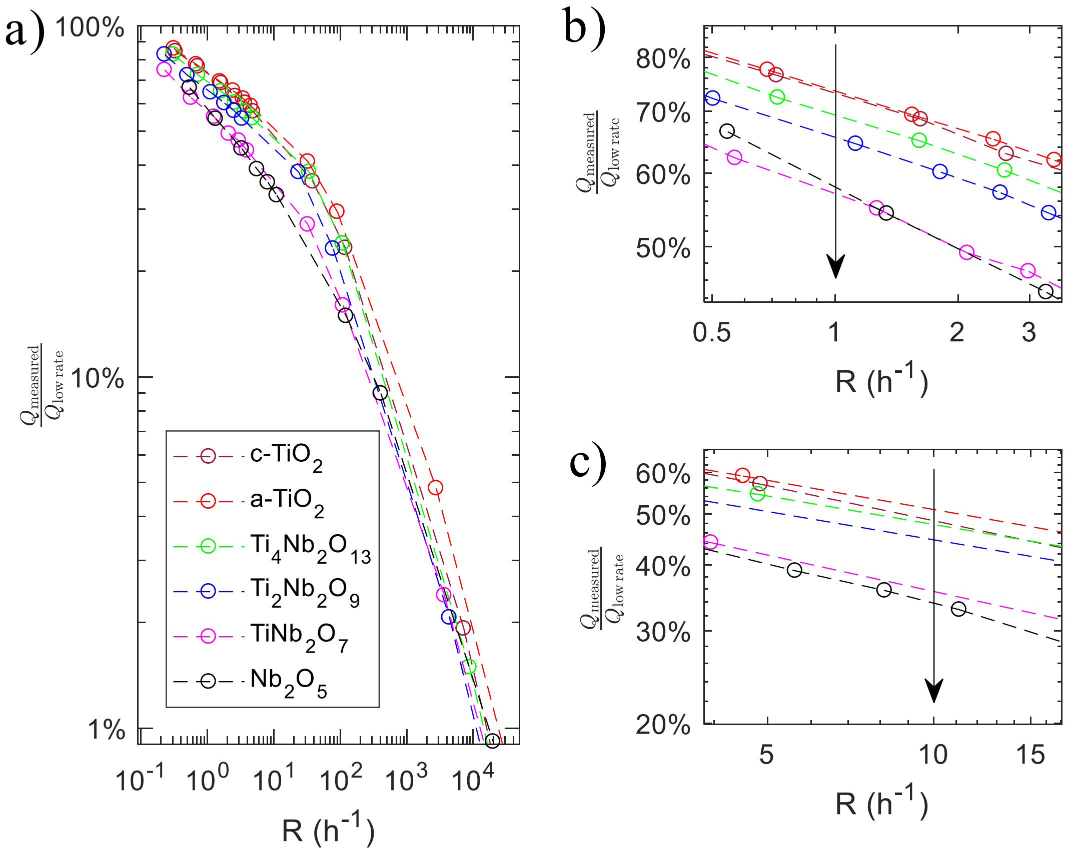

Fig. 9. Capacity retention as a function of $\bar{\boldsymbol{R}}$, with $Q_{\text{low rate}}$ calculated as presented by Tian at al. [44], showing a) capacity retention data up to a cutoff of 1% retention, with detailed views of the capacity retention at: (b) a rate of 1 h^{-1}; and (c) a rate of 10 h^{-1}.

retain the most capacity, the binary oxides a-TiO$_2$, c-TiO$_2$ and a-Nb$_2$O$_5$ retain more capacity (1.9%, 1.5% and 1.4%, respectively) than the a-Ti$_4$Nb$_2$O$_{13}$, a-Ti$_2$Nb$_2$O$_9$ and a-TiNb$_2$O$_7$ films (1.3%, 1.1% and 1.2%, respectively). To determine why the rate behaviour differs between the films, a PITT analysis was performed with the data being analysed using the electroanalytical model detailed in section 2.5.

3.4. Kinetic insights gained from PITT analysis and correlations with rate analysis

To determine which physical processes affect the rate capability of the TNO thin film electrodes, the PITT method was used to determine the electrochemical parameters R_{Ω}, R_{ct}, R_{D}, C_{EDL} and D_{chem}

Table 3
Comparison between the median, minimum, and maximum fitted values of the electrochemical parameters R_{Ω}, R_{ct}, R_D, C_{EDL} and D_{chem} for a-TiO$_2$, determined by fittting PITT and EIS experimental data with Eqs. (4) and (S1), respectively.

Electrochemical Method	R_{Ω} (Ω)	R_{ct} (Ω)	R_D (Ω)	C_{EDL} (μF)	D_{chem} (cm^2 s^{-1})
PITT	2.8 [2.0,3.2]	700 [210,1280]	1.3×10^4 [5.5×10^3, 6.2×10^4]	3.5 [2.3, 5.0]	2.2×10^{-13} [1.2×10^{-13}, 1.8×10^{-12}]
EIS	5.6 [4.0,6.4]	390 [180,1350]	8.0×10^3 [0.7×10^4, 2.4×10^5]	1.9 [1.1, 5.1]	1.7×10^{-11} [1.2×10^{-14}, 3.8×10^{-11}]

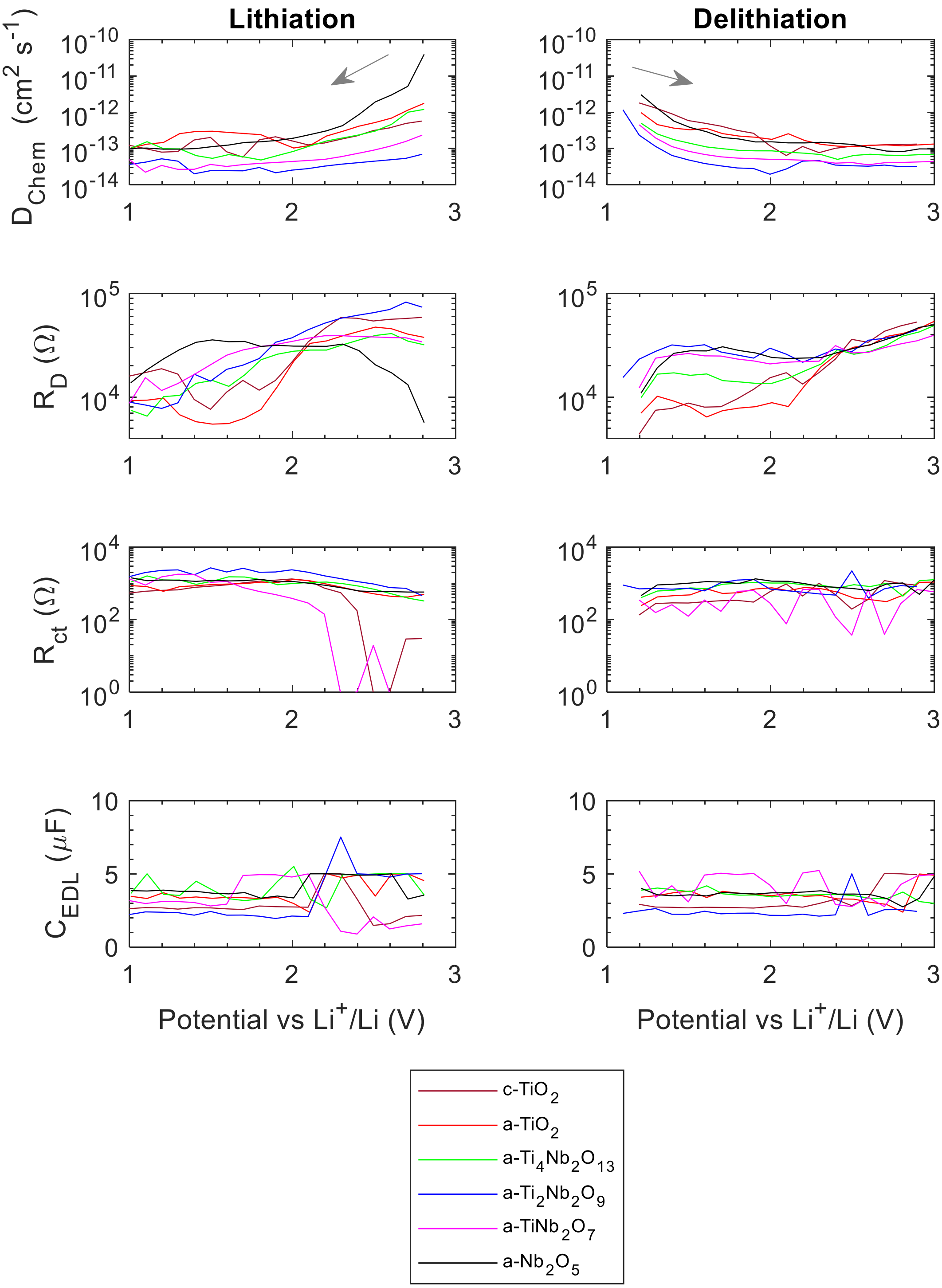

Fig. 10. Electrochemical parameters graphed as a functiuon of potential for lithiation (solid lines) and delithiation (dashed lines) determined by non-linear least squares regression of Eq. (4) onto the PITT experimental data as reported by Hall et al. [41].

Table 4
Pearson's correlation values between electrochemical parameters determined by PITT and the delithiation capacity at rates of 1, 10, 100, 1000 and 10,000 cycles h^{-1}.

Fitted Parameter (median)	**Capacity Retention**				
	@ 1 h^{-1}	**@ 10 h^{-1}**	**@ 100 h^{-1}**	**@ 1000 h^{-1}**	**@ 10,000 h^{-1}**
R_Ω	0.21	0.19	0.013	−0.023	−0.26
R_{ct}	0.030	0.032	−0.010	−0.034	−0.12
R_D	−0.87 *	−0.81 *	−0.93 *	−0.96 *	−0.85 *
C_{EDL}	−0.23	−0.28	−0.048	0.11	0.41
D_{chem}	0.51	0.34	0.55	0.78	0.94 *

* indicates p-value < 0.05.

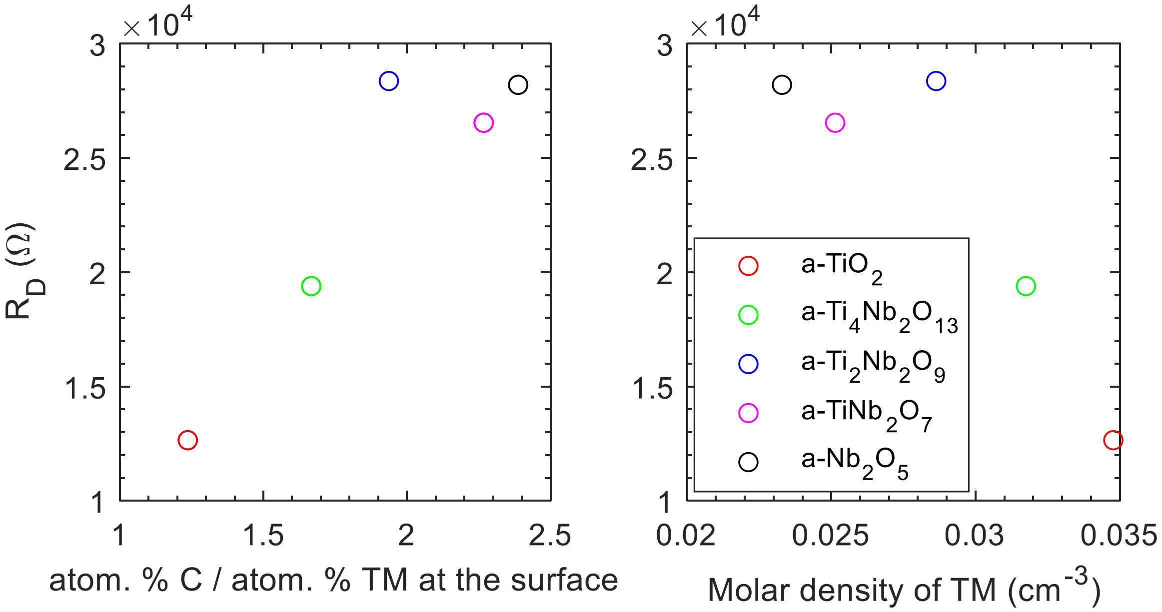

Fig. 11. Dependance of the electrocemical parameter R_D on phyicals properties of the thin films showing (left) the dependace on the amount (atomic%) of C on the surface with respect to the amount of transition metal (TM) on the surface, and (right) the dependance on the molar (volumetric) density of TMs. Both of these physical property are thought to relate to the number of insertion sites of the thin film. The ratio of C to TM on the surface was calculated from X-ray photoelectron spectroscopy. The molar density of TMs was calculated from density measurements from XRR.

across the 1.0 to 2.8 V potential range. To assess the reliability of the measurements, Table 3 compares the median values of these electrochemical parameters determined by PITT and by EIS for the a-TiO$_2$ electrode (see also Fig. S16). The estimated values of R_Ω, R_{ct}, R_D and C_{EDL} are similar within an order of magnitude between the methods. The value of C_{EDL}, in the order of one or several μF cm^{-2}, is lower by an order of magnitude than theoretical simulations of TiO$_2$ [61,62], however it is similar to reported areal double layer capacitances of other material systems [63]. Whilst the values of R_{ct} and R_D are orders of magnitude higher than that previously reported for a-TiO$_2$ electrodes, their normalised parameter Λ, defined by Montella as $\Lambda = R_D/(R_{ct} + R_\Omega)$ [42] is similar, with a median of 20 compared to a range of ~ 1–10 as previously reported [28,41]. Montella's assertion that this parameter Λ is indicative of the rate limiting step suggests that, as with previous reports, the a-TiO$_2$ film is rate limited by a mix of the insertion rate and diffusion of Li (i.e., under mixed control).

The median value of D_{chem}, as determined by fitting PITT and EIS data, varies by two orders of magnitude. Previous reports of the D_{chem} for a-TiO$_2$ place its value around 2.2 × 10^{-14} – 3.4 × 10^{-13} cm^2 s^{-1} [28], ~ 1 × 10^{-13} cm^2 s^{-1} [41] and 3.5 × 10^{-12} cm^2 s^{-1} [64]. This suggests that our estimates of D_{chem} from PITT are more consistent with previous reports than our estimates from EIS. This is attributed to the characteristic frequency of bounded diffusion, $f = D_{chem}/L$ [43], lying close to the minimum attainable frequency (see our discussion in section 3.1), and measurement instability at low frequencies making it difficult to meaningfully fit the low frequency regime in EIS.

The results of PITT analysis are shown in Fig. 10, which plots the fitted values of R_{ct}, R_D, D_{chem} and C_{EDL} as a function of potential during lithiation and delithiation for the TNO thin film electrodes. The fitted values of D_{chem} are also shown as a function of Li ion mole fraction, x, in Fig. S18. The estimated value of D_{chem} was similar for all TNO films, with median values (across the 1.0 to 2.8 V range) of 1.5 × 10^{-13} cm^2 s^{-1} for the c-TiO$_2$, and 2.2 × 10^{-13}, 8.7 × 10^{-14}, 3.5 × 10^{-14}, 4.7 × 10^{-14} and 1.5 × 10^{-13} cm^2 s^{-1} for the a-TiO$_2$, a-Ti$_4$Nb$_2$O$_{13}$, a-Ti$_2$Nb$_2$O$_9$, a-TiNb$_2$O$_7$ and a-Nb$_2$O$_5$, respectively. This suggests that diffusion is faster in a-TiO$_2$ and a-Nb$_2$O$_5$, and slower in the ternary oxides. The D_{chem} values for the a-TiNb$_2$O$_7$ are an order of magnitude lower than previously reported for pulsed laser deposition derived a-TiNb$_2$O$_7$ thin films [31], which may indicate that the structure of the sol gel derived a-TNO thin films impedes lithium diffusion.

Interestingly the magnitude of the D_{chem} values appears to be positively correlated to the capacity retention at a rate of 10,000 h^{-1} (see Fig. 9) but not at rates below 10,000 h^{-1}. This may indicate that diffusion occurs relatively quickly in all of the films relative to other processes, and as such isn't rate limiting at low and intermediate rates of charge and discharge. The values of R_D, which have a median value of 1.7 × 10^5, 1.3 × 10^4, 1.9 × 10^5, 2.8 × 10^5, 2.6 × 10^5 and 2.8 × 10^5 Ω for the c-TiO$_2$, a-TiO$_2$, a-Ti$_4$Nb$_2$O$_{13}$, a-Ti$_2$Nb$_2$O$_9$, a-TiNb$_2$O$_7$, respectively, however do inversely match the rate retention at rates of 1 and 10 h^{-1} (see Fig. 9b & c).

To assess correlation between the median values of the electrochemical parameters and the trends in rate retention presented in Fig. 9, correlation parameters are presented in Table 4. The only significant correlation (p-value < 0.05) at a rate of 1 and10 h^{-1} is seen to be R_D, which indicates that in the usable range of rates (that is, where the capacity retention is sufficiently high for practical charge storage), the most important factor is R_D. Given R_D is a composite of both R_{ct} and D_{chem} and the occupancy of surface sites (described in more detail in section 2), we interpret this to mean that the rate capability in inherently linked to the properties of the surface of the films as well as the diffusion of Li. Additionally, R_{ct} and D_{chem} by themselves show no correlation with the rate, which is in agreement with Λ values that suggest a mix of diffusion and charge transfer reaction control.

In order to provide a physical interpretation of R_D, we attempted to relate R_D to the physical properties of the films. We identified two properties which appear to be linked to R_D: (i) the ratio of the atomic% of C at the surface to the atomic% of transition metals at the surface (as determined via XPS), and (ii) the molar density of transition metals per unit volume (as determined via macroscopic density from XRR). The dependence of R_D on these parameters is shown in Fig. 11. Both of these physical properties are inherently linked to the number of transition metal atoms at the surface, and so this interpretation suggests that the rate retention in the a-TNO material system is linked to the density of Li insertion sites, and as such the insertion reaction more generally.

At rates of ~ 10,000 h^{-1}, where the order of rate retention changes, both R_D and D_{chem} are seen to have a significant correlation with the rate retention. This provides further evidence for our speculation that D_{chem} is sufficiently quick in the $<$ 100 nm thick films that it only affects the rate behaviour at unusably high rates. While this is useful for fundamentally understanding the rate behaviour of the TNO system, it is worth noting however that, even though the rate retention of a-TiO_2 is greater than any of the a-TNO films, the improvement of capacity that the a-TNO films show, particularly a-$Ti_2Nb_2O_9$, means that they provide higher gravimetric capacity at rates of up to 10C. Therefore, use of amorphous ternary mixed oxides can provide benefits over the more studied a-TiO_2 material system.

4. Conclusion

Amorphous TNO materials were investigated to assess their effectiveness as high rate Li ion battery anode materials. The TNO thin films were fabricated with atomic ratios of 2:1, 1:1 and 1:2 (Ti:Nb; $Ti_4Nb_2O_{13}$, $Ti_2Nb_2O_9$, $TiNb_2O_7$, respectively) via a sol gel method and were compared with anatase TiO_2, amorphous TiO_2 and amorphous Nb_2O_5. Use of thin films permitted the electrochemical properties of the films to be probed without interference from bulk diffusion or complex geometries. The TNO films achieved mean capacities between 717– 1039 mAh cm^{-3} over ten cycles at a current density of 0.2 A cm^{-3}, or between 231 and 335 mAh g^{-1} at a current density ~ 70 mA g^{-1}, when operating in the range of 1.0 to 3.0 V above the Li^+/Li potential. This exceeds the values of 175 mAh g^{-1} for Li titanate and 168 mAh g^{-1} for anatase TiO_2 (assuming in the latter case that 0.5 Li is inserted per unit formula). The D_{chem} values of the TNO materials were similar or greater than that of spinal lithium titanate; with median values of 8.7×10^{-14}, 3.5×10^{-14}, and 4.7×10^{-14} cm^2 s^{-1} for the amorphous $Ti_4Nb_2O_{13}$, $Ti_2Nb_2O_9$ and $TiNb_2O_7$, respectively. This fast Li diffusion highlights the potential for these amorphous TNO materials to be used for high rate electrochemical energy storage.

In the usable range of operation ($<$ 1 h^{-1} to up to 100 h^{-1}; i.e. de/lithiation occurs over ~1 h to 30 s), rate retention was sensitive to the amorphous film composition, with amorphous TiO_2 showing the greatest rate retention and amorphous Nb_2O_5 showing the poorest. The rate retention behaviour was compared to the electrochemical parameters determined via PITT. At rates of ~ 10 h^{-1} (i.e. de/lithiation occurs over 6 min), we observe that the mixed parameter R_D, which is related to both the charge transfer process and the diffusivity, shows the strongest relationship to rate retention. We interpret this result to mean that the insertion reaction and density of insertion sites dominates rate retention in a useably high rate of de/lithiation. At much higher rates (de/lithiation $<$ 1 s), Li diffusion appears to dominate. Despite amorphous TiO_2 showing the highest relative rate retention, in terms of the absolute capacities the amorphous $Ti_2Nb_2O_9$ and $TiNb_2O_7$ both outperform the amorphous TiO_2. The amorphous TNO system is hence a very promising material system for high rate Li ion batteries. Given that our results indicate that rate retention is sensitive to the density of insertion sites and the insertion reaction more generally, there exists the possibility to improve the rate performance via surface modifications or alternative synthesis routes.

Declaration of Competing Interest

The authors declare that they have no known conflict of interest.

Credit authorship contribution statement

Charles A. Hall: Conceptualization, Methodology, Formal analysis, Investigation, Writing – original draft. **Yu Jiang:** Investigation, Writing – review & editing. **Patrick A. Burr:** Methodology, Writing – review & editing. **Shujuan Huang:** Methodology, Writing – review & editing. **Zhi Li Teh:** Methodology, Investigation, Writing – review & editing. **Ivan Perez-Wurfl:** Methodology, Writing – review & editing. **Ning Song:** Investigation. **Alison Lennon:** Supervision, Writing – review & editing, Funding acquisition.

Acknowledgements

This work was supported by the Australian Research Council through Discovery Grant DP170103219 “Advanced Electrochemical Capacitors”. The first author acknowledges the Australian Government Research Program for providing a PhD scholarship. The authors thank Dr Bill Bin Gong and Dr Songyan Yin at the Solid State and Elemental Analysis Unit (MWAC), and Dr Yu Wang and Dr Daniel Sando at the X-Ray Diffraction Laboratory (MWAC), for the collection and fitting of XPS data and XRR data, respectively.

Supplementary materials

Supplementary material associated with this article can be found, in the online version, at doi:10.1016/j.electacta.2021.138544.

References

[1] Z.P. Cano, D. Banham, S. Ye, A. Hintennach, J. Lu, M. Fowler, Z. Chen, Batteries and fuel cells for emerging electric vehicle markets, Nat. Energy 3 (2018) 279–289.

[2] A. Lennon, Y. Jiang, C. Hall, D. Lau, N. Song, P. Burr, C.P. Grey, K.J. Griffith, High--rate lithium ion energy storage to facilitate increased penetration of photovoltaic systems in electricity grids, MRS Energy Sustain. 6 (2019) 4.

[3] Y. Jiang, J. Fletcher, P. Burr, C. Hall, B. Zheng, D.W. Wang, Z. Ouyang, A. Lennon, Suitability of representative electrochemical energy storage technologies for ramp-rate control of photovoltaic power, J. Power Sources 384 (2018) 396–407.

[4] K. Zaghib, M. Dontigny, A. Guerfi, P. Charest, I. Rodrigues, A. Mauger, C.M. Julien, Safe and fast-charging Li-ion battery with long shelf life for power applications, J. Power Sources 196 (2011) 3949–3954.

[5] W. Lu, C.M. López, N. Liu, J.T. Vaughey, A. Jansen, D. Dennis W, Overcharge effect on morphology and structure of carbon electrodes for lithium-ion batteries, J. Electrochem. Soc. 159 (2012) A566–A570.

[6] Q. Liu, C. Du, B. Shen, P. Zuo, X. Cheng, Y. Ma, G. Yin, Y. Gao, Understanding undesirable anode lithium plating issues in lithium-ion batteries, RSC Adv. 6 (2016) 88683–88700.

[7] L. Somerville, J. Bareño, S. Trask, P. Jennings, A. McGordon, C. Lyness, I. Bloom, The effect of charging rate on the graphite electrode of commercial lithium-ion cells: a post-mortem study, J. Power Sources 335 (2016) 189–196.

[8] K. Nakahara, R. Nakajima, T. Matsushima, H. Majima, Preparation of particulate $Li_4Ti_5O_{12}$ having excellent characteristics as an electrode active material for power storage cells, J. Power Sources 117 (2003) 131–136.

[9] C. Jiang, M. Wei, Z. Qi, T. Kudo, I. Honma, H. Zhou, Particle size dependence of the lithium storage capability and high rate performance of nanocrystalline anatase TiO_2 electrode, J. Power Sources 166 (2007) 239–243.

[10] H.T. Fang, M. Liu, D.W. Wang, T. Sun, D.S. Guan, F. Li, J. Zhou, T.K. Sham, H.M. Cheng, Comparison of the rate capability of nanostructured amorphous and anatase TiO_2 for lithium insertion using anodic TiO_2 nanotube arrays, Nanotechnology 20 (2009) 225701.

[11] G.N. Zhu, Y.G. Wang, Y.Y. Xia, Ti-based compounds as anode materials for Li-ion batteries, Energy Environ. Sci. 5 (2012) 6652.

[12] J.T. Han, Y.H. Huang, J.B. Goodenough, New anode framework for rechargeable lithium batteries, Chem. Mater. 23 (2011) 2027–2029.

[13] K.J. Griffith, I.D. Seymour, M.A. Hope, M.M. Butala, L.K. Lamontagne, M.B. Preefer, C.P. Kocer, G. Henkelman, A.J. Morris, M.J. Cliffe, S.E. Dutton, C.P. Grey, Ionic and electronic conduction in $TiNb_2O_7$, J. Am. Chem. Soc. 141 (2019) 16706–16725.

[14] K.J. Griffith, K.M. Wiaderek, G. Cibin, L.E. Marbella, C.P. Grey, Niobium tungsten oxides for high-rate lithium-ion energy storage, Nature 559 (2018) 556–563.

[15] S. Ouendi, C. Arico, F. Blanchard, J.L. Codron, X. Wallart, P.L. Taberna, P. Roussel, L. Clavier, P. Simon, C. Lethien, Synthesis of T-Nb_2O_5 thin-films deposited by atomic layer deposition for miniaturized electrochemical energy storage devices, Energy Storage Mater. 16 (2019) 581–588.

[16] S. Li, Q. Xu, E. Uchaker, X. Cao, G. Cao, Comparison of amorphous, pseudohexagonal and orthorhombic Nb_2O_5 for high-rate lithium ion insertion, CrystEngComm 18 (2016) 2532–2540.

[17] A.A. Voskanyan, M. Abramchuk, A. Navrotsky, Entropy stabilization of TiO_2–Nb_2O_5 Wadsley–roth shear phases and their prospects for lithium-ion battery anode materials, Chem. Mater. 32 (2020) 5301–5308.

[18] K.J. Griffith, A. Senyshyn, C.P. Grey, Structural stability from crystallographic shear in TiO_2-Nb_2O_5 phases: cation ordering and lithiation behavior of TiNb24O62, Inorg. Chem. 56 (2017) 4002–4010.

[19] H. Ding, Z. Song, H. Zhang, H. Zhang, X. Li, Niobium-based oxide anodes toward fast and safe energy storage: a review, Mater. Today Nano 11 (2020) 100082.

[20] L. Hu, L. Luo, L. Tang, C. Lin, R. Li, Y. Chen, Ti2Nb$_2$xO$_4$+5x anode materials for lithium-ion batteries: a comprehensive review, J. Mater. Chem. A 6 (2018) 9799–9815.

[21] S.R. Sivakkumar, J.Y. Nerkar, A.G. Pandolfo, Rate capability of graphite materials as negative electrodes in lithium-ion capacitors, Electrochim. Acta 55 (2010) 3330–3335.

[22] F. Wunde, F. Berkemeier, G. Schmitz, Lithium diffusion in sputter-deposited $Li_4Ti_5O_{12}$ thin films, J. Power Sources 215 (2012) 109–115.

[23] Y.H. Rho, K. Kanamura, Li+ ion diffusion in $Li_4Ti_5O_{12}$ thin film electrode prepared by PVP sol–gel method, J. Solid State Chem. 177 (2004) 2094–2100.

[24] J. Deng, Z. Lu, C.Y. Chung, X. Han, Z. Wang, H. Zhou, Electrochemical performance and kinetic behavior of lithium ion in $Li_4Ti_5O_{12}$ thin film electrodes, Appl. Surf. Sci. 314 (2014) 936–941.

[25] B. Babu, M.M. Shaijumon, Studies on kinetics and diffusion characteristics of lithium ions in $TiNb_2O_7$, Electrochim. Acta 345 (2020) 136208.

[26] J.F. Colin, V. Pralong, M. Hervieu, V. Caignaert, B. Raveau, Lithium insertion in an oriented nanoporous oxide with a tunnel structure: $Ti_2Nb_2O_9$, Chem. Mater. 20 (2008) 1534–1540.

[27] D. Pham-Cong, J. Kim, V.T. Tran, S.J. Kim, S.Y. Jeong, J.H. Choi, C.R. Cho, Electrochemical behavior of interconnected $Ti_2Nb_{10}O_{29}$ nanoparticles for high-power Li-ion battery anodes, Electrochim. Acta 236 (2017) 451–459.

[28] Y. Jiang, C. Hall, N. Song, D. Lau, P.A. Burr, R. Patterson, D.W. Wang, Z. Ouyang, A. Lennon, Evidence for fast lithium-ion diffusion and charge-transfer reactions in amorphous TiO x nanotubes: insights for high-rate electrochemical energy storage, ACS Appl. Mater. Interfaces 10 (2018) 42513–42523.

[29] S. Moitzheim, S. De Gendt, P.M. Vereecken, Investigation of the Li-ion insertion mechanism for amorphous and anatase TiO_2thin-films, J. Electrochem. Soc. 166 (2019) A1–A9.

[30] C. Deng, M.L. Lau, C. Ma, P. Skinner, Y. Liu, W. Xu, H. Zhou, X. Zhang, D. Wu, Y. Yin, Y. Ren, J. Perez, D. Jaramillo, P. Barnes, D. Hou, M. Dahl, B. Williford, C. Zheng, H. Xiong, A mechanistic study of mesoporous TiO_2 nanoparticle negative electrode materials with varying crystallinity for lithium ion batteries, J. Mater. Chem. A 8 (2020) 3333–3343.

[31] V. Daramalla, G. Venkatesh, B. Kishore, N. Munichandraiah, S.B. Krupanidhi, Superior electrochemical performance of amorphous titanium niobium oxide thin films for Li-Ion thin film batteries, J. Electrochem. Soc. 165 (2018) A764–A772.

[32] M.Z. Atashbar, H.T. Sun, B. Gong, W. Wlodarski, R. Lamb, XPS study of Nb–doped oxygen sensing TiO_2 thin films prepared by sol-gel method, Thin Solid Films 326 (1998) 238–244.

[33] K. Schenk-Meuser, D. Velten, E. Eisenbarth, V. Biehl, H. Duschner, J. Breme, XPS analysis of sol-gel-generated mixed-oxide layers for biomedical application, Surf. Interface Anal. 34 (2002) 59–62.

[34] D. Velten, E. Eisenbarth, N. Schanne, J. Breme, Biocompatible Nb_2O_5 thin films prepared by means of the sol–gel process, J. Mater. Sci. Mater. Med. 15 (2004) 457–461.

[35] M.C. Chang, C.S. Huang, Y.D. Ho, C.L. Huang, Sol-gel derived $TiNb_2O_7$ dielectric thin films for transparent electronic applications, J. Am. Ceram. Soc. 101 (2018) 674–682.

[36] K. Siwińska-Stefańska, J. Zdarta, D. Paukszta, T. Jesionowski, The influence of addition of a catalyst and chelating agent on the properties of titanium dioxide synthesized via the sol–gel method, J. Sol gel Sci. Technol. 75 (2015) 264–278.

[37] M. Von Heimendahl, Precipitation in aluminum-gold, Acta Metall. 15 (1967) 1441–1452.

[38] P. Walker, W.H. Tarn, CRC Handbook of Metal Etchants, CRC Press, 1990.

[39] a.W Weppner, R.A. Huggins, Electrochemical methods for determining kinetic properties of solids, Annu. Rev. Mater. Sci. 8 (1978) 269–311.

[40] C.J. Wen, B.A. Boukamp, R.A. Huggins, W. Weppner, Thermodynamic and mass transport properties of "LiAl, J. Electrochem. Soc. 126 (1979) 2258.

[41] C.A. Hall, A. Ignjatovic, Y. Jiang, P.A. Burr, A. Lennon, Time domain modelling of concurrent insertion and capacitive storage using Laplace domain representations of impedance, J. Electroanal. Chem. 850 (2019) 113379.

[42] C. Montella, Discussion of the potential step method for the determination of the diffusion coefficients of guest species in host materials: part I. Influence of charge transfer kinetics and ohmic potential drop, J. Electroanal. Chem. 518 (2002) 61–83.

[43] J.S. Chen, J.P. Diard, R. Durand, C. Montella, Hydrogen insertion reaction with restricted diffusion. Part 1. potential step—EIS theory and review for the direct insertion mechanism, J. Electroanal. Chem. 406 (1996) 1–13.

[44] R. Tian, S.H. Park, P.J. King, G. Cunningham, J. Coelho, V. Nicolosi, J.N. Coleman, Quantifying the factors limiting rate performance in battery electrodes, Nat. Commun. 10 (2019) 1933.

[45] S.G. Pawar, M.A. Chougule, D.S. Dalavi, P.S. Patil, A.V. Moholkar, S. Sen, J.H. Kim, V.B. Patil, Effect of annealing on microstructural and optoelectronic properties of nanocrystalline TiO_2 thin films, J. Exp. Nanosci. 8 (2012) 500–508.

[46] R. Kužel, L. Nichtová, Z. Matěj, J. Musil, *In-situ* X-ray diffraction studies of time and thickness dependence of crystallization of amorphous TiO_2 thin films and stress evolution, Thin Solid Films 519 (2010) 1649–1654.

[47] R. Kužel, L. Nichtová, Z. Matěj, D. Heřman, J. Šícha, J. Musil, in: Tenth European Powder Diffraction Conference, Study of Crystallization of Magnetron Sputtered TiO2 Thin Films by X-ray Scattering, De Gruyter, 2007, p. 247.

[48] R. Kužel, L. Nichtová, Z. Matěj, Z. Hubička, J. Buršík, X-ray diffraction investigations of TiO_2 thin films and their thermal stability, MRS Proc. 1352 (2011) 57–62.

[49] F. Guillemot, M.C. Porte, C. Labrugere, C. Baquey, Ti4+ to Ti3+ conversion of TiO_2 uppermost layer by low-temperature vacuum annealing: interest for titanium biomedical applications, J. Colloid Interface Sci. 255 (2002) 75–78.

[50] V.V. Atuchin, I.E. Kalabin, V.G. Kesler, N.V. Pervukhina, Nb 3d and O 1s core levels and chemical bonding in niobates, J. Electron Spectros Relat Phenom. 142 (2005) 129–134.

[51] N. Özer, T. Barreto, T. Büyüklimanli, C.M. Lampert, Characterization of sol-gel deposited niobium pentoxide films for electrochromic devices, Sol. Energy Mater. Sol Cells 36 (1995) 433–443.

[52] N. Özer, M.D. Rubin, C.M. Lampert, Optical and electrochemical characteristics of niobium oxide films prepared by sol-gel process and magnetron sputtering A comparison, Sol. Energy Mater. Sol. Cells 40 (1996) 285–296.

[53] N. Özer, D.G. Chen, C.M. Lampert, Preparation and properties of spin-coated Nb_2O_5 films by the sol-gel process for electrochromic applications, Thin Solid Films 277 (1996) 162–168.

[54] R. Romero, J.R. Ramos-Barrado, F. Martin, D. Leinen, Nb_2O_5 thin films obtained by chemical spray pyrolysis, Surf. Interface Anal. 36 (2004) 888–891.

[55] J. Wang, J. Polleux, J. Lim, B. Dunn, Pseudocapacitive contributions to electrochemical energy storage in TiO_2 (anatase) nanoparticles, J. Phys. Chem. C 111 (2007) 14925–14931.

[56] J.S. Chen, X.W. Lou, Anatase TiO_2 nanosheet: an ideal host structure for fast and efficient lithium insertion/extraction, Electrochem. Commun. 11 (2009) 2332–2335.

[57] S.S. El-Deen, A.M. Hashem, A.E. Abdel Ghany, S. Indris, H. Ehrenberg, A. Mauger, C.M. Julien, Anatase TiO_2 nanoparticles for lithium-ion batteries, Ionics 24 (2018) 2925–2934.

[58] M. Hibino, K. Abe, M. Mochizuki, M. Miyayama, Amorphous titanium oxide electrode for high-rate discharge and charge, J. Power Sources 126 (2004) 139–143.

[59] H. Furukawa, M. Hibino, I. Honma, Electrochemical properties of nanostructured amorphous, sol-gel-synthesized TiO_2/acetylene black composite electrodes, J. Electrochem. Soc. 151 (2004) A527.

[60] C. Costentin, Electrochemical energy storage: questioning the popular v/v(1/2) scan rate diagnosis in cyclic voltammetry, J. Phys. Chem. Lett. 11 (2020) 9846–9849.

[61] J. Cheng, M. Sprik, The electric double layer at a rutile TiO_2 water interface modelled using density functional theory based molecular dynamics simulation, J. Phys. Condens. Matter. 26 (2014) 244108.

[62] C. Zhang, J. Hutter, M. Sprik, Coupling of surface chemistry and electric double layer at TiO_2 electrochemical interfaces, J. Phys. Chem. Lett. 10 (2019) 3871–3876.

[63] J. Chmiola, G. Yushin, Y. Gogotsi, C. Portet, P. Simon, P.L. Taberna, Anomalous increase in carbon capacitance at pore sizes less than 1 nanometer, Science 313 (2006) 1760–1763.

[64] W.J.H. Borghols, D. Lützenkirchen-Hecht, U. Haake, W. Chan, U. Lafont, E.M. Kelder, E.R.H. van Eck, A.P.M. Kentgens, F.M. Mulder, M. Wagemaker, Lithium storage in amorphous TiO_2 nanoparticles, J. Electrochem. Soc. 157 (2010) A582.